# Generating porosity during olivine carbonation via dissolution channels and expansion cracks

Tiange Xing[1], Wenlu Zhu[1], Florian Fusseis[2], Harrison Lisabeth [1,3]

[1] Department of Geology, University of Maryland, College Park, 20742, USA

[2] School of Geosciences, University of Edinburgh, Edinburgh, EH9 3FE, UK

[3] Department of Geophysics, Stanford University, Stanford, 94305, USA

*Correspondence to*: Tiange Xing (tiange@umd.edu)

**Abstract.** The olivine carbonation reaction, in which carbon dioxide is chemically incorporated to form carbonate, is central to the emerging carbon sequestration method using ultramafic rocks. The rate of this retrograde metamorphic reaction is controlled, in part, by the available reactive surface area: as the solid volume increases during carbonation, the feasibility of this method ultimately depends on the maintenance of porosity and the creation of new reactive surfaces. We conducted in-situ dynamic X-ray microtomography and nanotomography experiments to image and quantify the porosity generation during olivine carbonation. We designed a sample setup that included a thick-walled cup (made of porous olivine aggregates with a mean grain size of either ~5 or ~80 μm) filled with loose olivine sands with grain sizes of 100-500 μm. The whole sample assembly was reacted with a NaHCO₃ aqueous solution at 200 °C, under a constant confining pressure of 13 MPa and a pore pressure of 10 MPa. Using synchrotron-based X-ray microtomography, the 3-dimensional (3-D) pore structure evolution of the carbonating olivine cup was documented until the olivine aggregates became disintegrated. The dynamic microtomography data show a volume reduction in olivine at the beginning of the reaction, indicating a vigorous dissolution process consistent with the disequilibrium reaction kinetics. In the olivine cup with a grain size of ~80 μm (coarse-grained cup), dissolution planes developed within 30 hours, before any precipitation was observed. In the experiment with the olivine cup of ~5 μm mean grain size (fine-grained cup), idiomorphic magnesite crystals were observed on the surface of the olivine sands. The magnesite shows a near constant growth throughout the experiment, suggesting that the reaction is self-sustained. Large fractures were generated as reaction proceeds and eventually disintegrate the aggregate after 140 hours. Detailed analysis show that these are expansion cracks caused by the volume mismatch in the cup walls, between the expanding interior and the near-surface which keeps a nearly constant volume. Nanotomography images of the reacted olivine cup reveal pervasive etch-pits and worm-holes in the olivine grains. We interpret this perforation of the solids to provide continuous fluid access, which is likely key to the complete carbonation observed in nature. Reactions proceeding through the formation of nano- to micron-scale dissolution channels provide a viable microscale mechanism in carbon sequestration practices. For the natural peridotite carbonation, a coupled-mechanism of dissolution and reaction-induced fracturing should account for the observed self-sustainability of the reaction.

## 1 Introduction

Mantle peridotites are exposed widely on the Earth's surface in tectonic settings such as mid-ocean ridges, subduction zones and ophiolites (Escartín et al., 1997; Fryer et al., 1995). Peridotite is mainly composed of olivine which is unstable at temperature below 700 °C in the presence of water (Evans, 1977), and below 500 °C in the presence of CO2-rich fluids (Johannes, 1969). The transformation of olivine to serpentine and carbonates due to fluid-rock interaction is extensively

observed in peridotite outcrops (e.g. Beinlich et al., 2012; Falk and Kelemen, 2015; Hansen et al., 2005). Rock deformation experiments have demonstrated that fluid alteration to peridotite can strongly affect the strength and tectonics of the oceanic lithosphere (Deschamps et al., 2013; Moore et al., 1996). Therefore, study of the olivine-fluid interaction is of great importance in understanding the alteration process of peridotite in a variety of tectonic regions. General peridotite alteration reactions can
40   be formulated as follow (Hansen et al., 2005; Kelemen and Matter, 2008):

Olivine $+$ $CO_2$ in fluid $=$ Magnesite $+$ Quartz,
$$Mg_2SiO_4 + 2CO_2 = 2MgCO_3 + SiO_2, \tag{1}$$

Olivine $+$ $CO_2$ in fluid $+ H_2O =$ Talc $+$ Magnesite,
$$4Mg_2SiO_4 + 5CO_2 + H_2O = Mg_3Si_4O_{10}(OH)_2 + 5MgCO_3, \tag{2}$$

45   Olivine $+ H_2O =$ Serpentine $+$ Brucite,
$$2Mg_2SiO_4 + 3H_2O = Mg_3Si_2O_5(OH)_4 + Mg(OH)_2, \tag{3}$$

Brucite $+ CO_2 =$ Magnesite $+$ $H_2O$,
$$Mg(OH)_2 + CO_2 = MgCO_3 + H_2O, \tag{4}$$
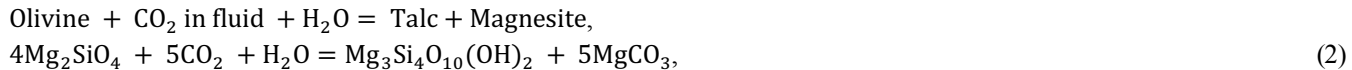
Although peridotite weathering reactions occur widely in nature, the rate of olivine carbonation at subsurface conditions is
50   debated. Since the retrograde metamorphic reactions are kinetically fast, the extent of transformation is limited by fluid supply which depends on the accessible fluid pathways. As the hydration and carbonation of olivine results in an up to ~44% increase in solid molar volume (Goff and Lackner, 1998; Hansen et al., 2005; Kelemen and Matter, 2008), carbonation of olivine is generally assumed to be self-limiting: the reaction products would gradually fill up the pore space and lead to a decrease in the porosity (Emmanuel and Berkowitz, 2006; Hövelmann et al., 2012), which in turn lowers permeability and reduces fluid
55   supply. This negative feedback would ultimately force the alteration to cease. However, naturally occurring completely carbonated peridotites are evidence that these limitations can be overcome. For instance, listvenite is the natural completely carbonated product of peridotite, which is composed of magnesite, quartz and trace minerals (Beinlich et al., 2012; Nasir et al., 2007). This creates a conundrum of how the large extent carbonation can be achieved with the potential self-limitation of reducing fluid pathways.

60   In order to explain this discrepancy between the theory and the observation, numerous studies have been conducted aiming to find a mechanism to maintain the access for reacting fluid during olivine alteration reactions. In 1985, Macdonald and Fyfe examined naturally altered peridotite and proposed that the large volume change associated with the reaction could generate high local stresses and strains, which would cause episodic cracking. This idea has then been applied to olivine carbonation by Kelemen and Matter (2008), who proposed a positive feedback loop where fractures could be generated during the volume-
65   expanding reaction, porosity and permeability can be maintained or even increased, which in turn would accelerate the carbonation processes (cf. Rudge et al., 2010). In 2011, Kelemen et al. showed that in natural peridotites cross-cutting hierarchical fracture networks filled by syn-kinematic carbonate and quartz veins extend to microscopic scales. These cross-cutting networks indicate coeval carbonate crystallization and fracturing. Several studies also showed that the forces generated by the volume increase should be enough to fracture peridotite (Iyer et al., 2008; Jamtveit et al., 2009, 2011; Ulven et al.,
70   2014).

While reaction-induced fracturing is accepted as a way to maintain fluid access, the mechanical details of the process are poorly understood. As for the mechanism that generates stresses, 'crystallization pressure' (also termed 'force of

crystallization') has been proposed (e.g. Scherer, 2004; Weyl, 1959; Winkler and Singer, 1972). In this model, the precipitation/crystallization of reaction products exert pressure around the growing crystals, and fracturing takes place when that pressure exceeds the local minimum principal stress (Kelemen and Hirth, 2012). Salt crystallization (Scherer, 2004) is a common example where high crystallization forces due to the nucleation of precipitates in pore space cause samples to 'burst from the inside' (see Figure 1a). However, studies have shown that the crystallization force is low in the olivine carbonation system (e.g. van Noort et al., 2017). Because of the lack of experimental evidence of crystallization forces during olivine alteration, Zhu et al. (2016) proposed an 'expansion cracking' mechanism as an alternative model after successfully producing reaction-induced fractures in an in-situ synchrotron X-ray microtomography study. In the 'expansion cracking' model, tensile stresses are generated due to the volume mismatch between regions with different precipitation rates, leading to cracks forming in regions that expand slower than their surroundings (see Figure 1b).

Beyond fracturing, dissolution has been recognized as an important part of the olivine alteration process (e.g. Velbel, 2009; Velbel and Ranck, 2008; Wilson and Jones, 1983) and proposed as a mechanism to explain the observed complete carbonation of peridotite. In 1978, Grandstaff showed that dissolution could significantly increase the surface area through etch-pitting. Wilson (2004) suggested that the weathering of olivine is controlled by etch-pitting and channel formation due to preferential dissolution, which assists the migration of fluid and promote further reaction. Andreani et al. (2009) suggested that permeability may be maintained during peridotite carbonation by the development of preferential flow zones. Lisabeth et al. (2017a, 2017b) observed relevant structures in dunite samples that have been reacted under controlled stress conditions, and interpreted them as a pattern of secondary porosity bands formed by dissolution coupled to locally intensified compressional stresses.

Previous investigations of olivine carbonation were largely based on the interpretation of naturally deformed samples (e.g. Macdonald and Fyfe, 1985), thermodynamic modelling (e.g. Kelemen and Hirth, 2012) or comparison with reaction systems other than olivine (e.g. leucite to analcime in Jamtveit et al., 2009). While these approaches led to significant advancements, there are limitations to the understanding of the mechanisms responsible for porosity generation during olivine carbonation that these approaches can provide. The history of natural fault rocks is inevitably complex, and thermodynamic arguments and numerical models can only indicate a potential, while the actual progress of chemical reactions is strongly affected by interfacial structures, which vary considerably in different mineral systems. Thus, it is critical to complement such studies with laboratory experiments on olivine carbonation.

Synchrotron-based X-ray tomography is an advanced non-destructive method to capture three-dimensional images of materials. Where processes affecting these materials are followed through time, a 4-dimensional (3 spatial dimensions + time) dataset is captured. By using X-ray transparent reaction cells (Fusseis et al., 2014b), the technique enables the investigation of fluid-rock interaction at controlled and geologically relevant conditions. We examined the carbonation process of olivine on the basis of 4-dimensional images acquired by X-ray microtomographic imaging with synchrotron radiation at the Advanced Photon Source. Zhu et al. (2016) hypothesized that large grains would be preferred sites for precipitation of new crystals, and the contrast in the grain size produced the volume mismatch due to a preferred precipitation on the larger grains and led to the fracturing of the sample. To further test the hypothesis, in this current study, we conducted a new experiment using an olivine aggregate with larger grain size (80-100 μm) compared to the previous experiment reported by Zhu et al., (2016; 0-20 μm). We also performed advanced 3D analyses and quantification of the micro- and nano-tomography data obtained by Zhu et al. (2016). In an advancement of the results presented by Zhu et al. (2016), here we present direct evidence for the coupled mechanisms of dissolution and precipitation-driven fracturing during olivine carbonation and demonstrate their importance in sustaining the reaction progress at different spatial and temporal scales. We further show direct evidence of how reaction-induced fracturing operates, i.e. how stress is generated through volume-increasing reactions. A better understanding of olivine

carbonation directly applies to the geological sequestration of $CO_2$ (Gislason et al., 2010; Mani et al., 2008). The principle of
in-situ carbon mineralization is the conversion of silicate and hydroxide minerals to form carbonate minerals as a stable sink
for $CO_2$ (Power et al., 2013). Peridotite, because of its wide occurrence and high reactivity, is considered one of the best
potential feedstocks for $CO_2$ mineralization (Andreani et al., 2009; Beinlich and Austrheim, 2012); the estimated rate of $CO_2$
consumption peridotite carbonation could be as high as $2\times10^9$ tons·km$^{-3}$ per year (Kelemen and Matter, 2008). As the dominant
constituent of peridotite, olivine becomes the most important mineral for $CO_2$ mineralization. Our study provides new insights
into carbon sequestration using ultramafic rocks, and our findings on the mechanism of fracture generation during olivine
carbonation could provide guidance to industrial applications.

## 2 Experimental Setup

### 2.1 Sample Configuration

In Zhu et al. (2016), the contrast in grain size between the loose grains and the cup wall aggregate is hypothesized as the cause
of the non-uniform precipitation which is crucial to the generation of fractures in the experiment. Here, we use coarse-grained
olivine aggregate in the cup wall to reduce the contrast in grain size between the cup wall and the fillings and further test their
hypothesis.

The sample assembly consists of a millimeter-sized synthesized San Carlos olivine cup, filled with loose San Carlos olivine
sand (grain size 100-500 μm, see Figure 2a) and then covered by a lid made of the same material as the cup. Both the olivine
cup and its lid are taken from a sintered pellet made from pulverized San Carlos olivine with a grain size of 80-100 μm. This
coarse-grained olivine cup is referred to as large grain cup (LGC) in the following discussion. Data obtained from the LGC
experiment will be compared to the results of an olivine carbonation experiment conducted by Zhu et al. (2016) at the same
experimental conditions, on a fine-grained (grains sizes between 0-20 μm) cup. The fine-grained olivine cup is referred to as
small grain olivine cup (SGC) in the following discussion.

The cup, which was fabricated by hot-pressing in a procedure described in Zhu et al. (2016), has inner and outer diameters of
1 and 1.8 mm respectively, with a resulting wall thickness of ~0.4 mm. The initial porosity of the cup is ~10%. Both LGC and
SGC samples were sintered for 4 hours at 1400**°C**, the LGC sample came out weaker (less cohesive) compared to the SGC
sample, and the initial porosity of LGC is slightly higher than that of SGC.

The loose grains inside the cup allowed the inspection of magnesite growth on free olivine surfaces. The sample assemblies
(i.e., olivine cup + loose grains) were jacketed and loaded into an X-ray transparent pressure cell (Figure 3). A confining
pressure of 13 MPa and a pore fluid of $NaHCO_3$ aqueous solution (1.5 mol·L$^{-1}$) at 10 MPa were applied to the sample. The
pore pressure downstream is regulated by a pressure regulator while the upstream is controlled by a syringe pump to form a
semi-open system. Both upstream and downstream pore pressures were maintained at 10MPa throughout the experiment. A
small axial load is applied independently from the confining pressure by locking the piston at a fixed position. The pressure
cell was then heated to 200 °C to initiate the reaction. These conditions were kept constant during the entire microtomography
experiment. The reaction of the LGC sample was stopped at 36 hours after considerable secondary porosity generation was
observed. No magnesite precipitation was detected in LGC. The SGC sample was reacted for 7 days until intense fracturing
was observed. Significant magnesite precipitation was detected in SGC (Zhu et al., 2016).

**2.2 Micro- and Nano-tomography**

150    Third-generation synchrotron facilities produce electromagnetic radiation bright enough to allow rapid imaging even inside experimental vessels, thereby enabling studies of dynamic processes ranging over periods from seconds to days, while acquiring individual 3-dimensional (3-D) data sets in fractions of a second. Synchrotron X-ray microtomography has therefore become one of the most powerful tools in structural geology and rock mechanics studies (see Fusseis et al., 2014a for a review and Bedford et al., 2017 for a recent application).

155    In this experiment, synchrotron-based X-ray absorption microtomography has been used to record the dynamic carbonation of olivine in 4 dimensions. We used an X-ray transparent cell (Fusseis et al., 2014b), mounted in the upstream experimental station at beamline 2BM of the Advanced Photon Source of Argonne National Laboratory, 25 m from the source. There, a polychromatic beam filtered by 1 mm aluminum, 15 mm silicon and 8 mm borosilicate glass yielded a photon flux with an energy peak at 65 KeV (Zhu et al., 2016). A Cooke pco.edge sCMOS camera with 2560×2160 pixels (pixel size 6.5×6.5 μm$^2$)

160    was used in a flying scan mode. The sample-detector distance was 300 mm, which introduced a clear phase contrast signal to the data (Cloetens et al., 1996). The camera recorded projections from a 10 μm thick LuAG:Ce single crystal scintillator, magnified through a 10× Mitutoyo long-working distance lens yielding a pixel size of 0.65 μm. Projections were collected with an exposure time of 50 ms while the sample was rotated over 180 ° with 1.2 °·s$^{-1}$. 1500 projections were collected in 150 s. For the LGC sample, 115 3-D microtomographic data sets were acquired over 36 hours, together forming a 4D data set,

165    with time as the fourth dimension. For the SGC sample, 379 data sets were acquired over 7 days. From these 379 datasets, 19 were chosen for further detailed quantitative analysis. All acquired microtomographic data were reconstructed using the code Tomopy (Gürsoy et al., 2014) into stacks of 2160 images each, with dimensions of 2560×2560 pixels per image. Each of these image stacks contains a 3-dimensional representation of the sample mapped onto a 32-bit image, with the grey values reflecting the local absorption of X-rays (Fusseis et al., 2014a). Where the refractive indices change in the sample, i.e. on edges, this

170    absorption signal is locally overlain by a phase contrast signal (Cloetens et al., 1996). The time series dataset covers the entire duration of the experiment.

After the in-situ acquisition of the microtomography images, a fragment of the cup wall from the SGC was taken to conduct nano-scale imaging. Nanotomography was conducted using a transmission X-ray microscope (TXM) at the beamline 32-ID of the Advanced Photon Source of Argonne National Laboratory. A monochromatic beam of X-ray with an energy of 8 keV was

175    used. An X-ray objective lens corresponding to a Fresnel zone plate with 60nm outermost zone width was used to magnify radiographs onto a detection system assembly comprising a LuAG scintillator, a Zeiss 5X optical microscope objective lens and an Andor Neo sCMOS camera. Nanotomography yields a pixel size of ~60 nm after binning.

**2.3 Image Processing Procedures**

Zhu et al. (2016) conducted preliminary analyses and measurements on 2-dimensional (2-D) image slices (see Figure 2b) of

180    SGC through the 3-D microtomography datasets acquired. Here, we present the results of a true 3-D volume quantification of the microstructural changes in the SGC sample (i.e., spatio-temporal changes in grain and pore volumes) and compared them with the results obtained from LGC sample in this study.

In both the SGC and the LGC samples, a sub-region that included both, the cup wall near-surface as well as the cup wall's interior was chosen for detailed inspection from all datasets. For each sample, two subvolumes with the dimension of

185    400×400×400 voxels were cropped out from the region of interests in the cup wall (see Figure 4, subvolume 1 and 2 from SGC

and subvolume 3 and 4 from LGC). In the SGC sample, subvolume 2 was further cropped to a volume of 247×400×400 voxels (160.55×260×260 μm$^3$) to eliminate the boundary of the cup wall.

Image segmentation is the separation and extraction of phases of interests from the 3-D data sets for further analysis and quantification. A large range of segmentation algorithms exist (e.g. Kaestner et al., 2008). In global binary thresholding, images are segmented by identifying the grey value range representing a phase and assigning all voxels within that range a single value (usually 1) while all other voxels are classified as matrix (and assigned a different single value, usually 0) (Heilbronner and Barrett, 2014). Global binarization was conducted in Avizo Fire 8 to isolate pores from solids.

In the SGC sample, at the given spatial resolution, we could not resolve the new crystals precipitated within the cup wall and only the pore space was segmented there. Pixels with grey values that fall in the range (-0.00031, -0.000077) were assigned to pore space. We used the segmented data to quantify the change in the spatial distribution of pores during the experiment. Each subvolume was further divided into smaller cubes (side lengths ~26 μm) in which the average porosity is calculated to examine where changes in porosity occurred. In the LGC sample, grey values that fall in the range (-0.00031, -0.000095) were assigned to pore space.

In the nanotomography data, the grey value range between (2.97672×10$^{-9}$, 0.13161) was assigned to pore space. In these data, the olivine is represented by grey values between (0.30846, 1.3161). Voxels with intermediate grey values (0.13161, 0.30846) were assigned to reaction precipitates (e.g. magnesite).

## 3 Data analysis and results

We have observed the development of secondary porosity during the reaction in both the LGC and SGC experiments (Figure 5). Detailed examination has further revealed that the porosity generation in LGC is significant different from that in SGC.

### 3.1 Dissolution in the LGC sample

As reaction proceeded, olivine grains in the LGC sample shrank in size and secondary pores were produced (Figure 5a). This suggests that dissolution dominated the carbonation reaction in LGC, with little precipitation detected. The secondary pore space formed first at the center of the cup wall and grew outwards (Figure 5a), which is opposite to that in SGC where fractures grew from the surface of cup wall inwards (Figure 5b).

Planar fractures formed within 36 hours of reaction in LGC (Figure 6), and the experiment was stopped shortly after the formation of these fractures. Because of the lack of precipitation, these planar fractures could not be induced by the non-uniform volume expansion as in the SGC sample (Zhu et al., 2016). Under a constant confining pressure, volume reduction in olivine grains (i.e., dissolution) likely shortened the LGC sample length as reaction proceeded. Because the axial piston was kept at a fixed position during the experiment, this shortening in sample length resulted a decrease in axial stress. Because the LGC sample is mechanically weak (less cohesion), even though the reduction in axial stress is small, it could be sufficient to cause fracture LGC in the manner of dilation bands under triaxial extension (e.g., Zhu et al., 1997). Detailed examination of the 3D images revealed the disappearance of small grains along the plane which is clear evidence of dissolution. Thus we refer to these planar cracks as dissolution-assisted fractures under triaxial extension. The dissolution-assisted fractures were not observed in the SGC sample because it is much stronger owing to its fine grain size (e.g. Eberhardt et al., 1999; Singh, 1988). The triaxial extension stress condition would be no longer present once precipitation started (after ~36 hours) and sample volume expansion took place.

**3.2 Lack of precipitation in the LGC sample**

Evidences from direct observation and quantitative analysis have shown that the LGC sample is lack of precipitation.

Within the duration of the reaction, hardly any precipitation was observed in the cup wall. In the microtomographic images,
225  the surface layer of the loose olivine grains remained free of precipitates. Both sides of the cup wall remained straight and showed no spalling due to precipitation-caused non-uniform stretching. The sample did not experience any expansion as seen in the SGC sample.

Apart from the direct observation, grey value histograms of the data also show evidence of lacking precipitation in the LGC sample. The grey value histograms of 4D microtomography data evolve systematically during in-situ experiments, which can
230  be utilized in the evaluation of the reaction progress (Fusseis et al., 2012). Systematic analysis of the histograms of the grey value distribution revealed the progression of reaction during the experiment (Figure 7).

Comparing the histogram of SGC sample with the LGC sample, the shape of the histograms from the LGC sample (Figure 7a) is clearly asymmetric compared to the bell-shaped histograms in the SGC sample (Figure 7b). The slope on the precipitation side of the LGC histogram is steep and becomes steeper as reaction proceeds, indicating dissolution of olivine with little to no
235  precipitation. The slope on the pore side of the LGC histogram becomes shallower, owing to the secondary porosity generation due to the dissolution of olivine.

Data from the SGC sample showed that the histograms became uniformly flatter and wider over the duration of the experiment, with an increase in the number of both the darkest and brightest voxels at the expense of the voxels with intermediate grey values. These systematic changes in the absorption behaviour can only be caused by the sample reacting and indeed reflect the
240  dissolution of olivine, the generation of pore space and the precipitation of reaction products, in addition to phase contrast around newly generated edges in the sample. The best fit curves to the histograms evolved systematically during the reaction and intersected in a relatively narrow grey value range (-0.000077, -0.000055) (Figure 7). Voxels with grey values darker than -0.000077 correspond to fluid-filled pores, whose volume proportion increases throughout the reaction process.

**3.3 Porosity evolution of LGC compared to SGC**

245  Pore space development in LGC is significantly different from SGC. As shown in Figure 5 and 6, the secondary pore space in the LGC developed simultaneously at the interior and the near surface of the sample. However, in the SGC sample, pore space first occurred in area close to the surface and propagated inwards.

To further examine the difference in porosity generation of the LGC and SGC sample during the reaction, pore spaces within the subvolumes are segmented from the images and calculated. Figure 8 compares the porosity of subvolume 1 and 2 (Zhu et
250  al., 2016) from SGC and subvolume 3 and 4 from LGC samples. As shown by the figure, initial porosity of the LGC and SGC sample are similar. The rate of porosity increase in the LGC sample is similar to the SGC during the first 36 hours after the reaction started. Porosity of the LGC sample are increasing throughout the duration of the experiment while porosity of the SGC shows a decrease after 90 hours of reaction. In the LGC sample, the porosity increased ~5% and is likely resulted from dissolution. This is consistent with other studies that the precipitate do not occur in olivine carbonation within 36 hours of
255  reaction (e.g. Lisabeth et al., 2017a).

We then further evaluated the porosity distribution within the subvolumes by quantifying the porosity of 2D tangential slice along the samples' radial direction. Figure 9 compares the porosity distribution of subvolume 2 from the SGC sample with

subvolume 4 from the LGC sample. The subvolume 4 shows a homogeneous increase in porosity of ~5% throughout the entire subvolume. Subvolume 2, while showing an increase of porosity during the first 30 hours of the reaction, starts to show a porosity decrease in areas close to the center of the cup wall after 81 hours of reaction. Comparison of the subvolumes from SGC and LGC revealed that the porosity generation within the LGC sample is relatively homogeneous while the porosity generation within the SGC sample starts to show contrast between the cup's near surface and its interior after 81 hours of reaction. Results from the porosity evaluation further support that the LGC sample is dominated by dissolution with no presence of precipitation.

### 3.4 Fractures in LGC vs. SGC

As discussed in 3.1, the planar fractures observed in the LGC sample are likely a result of the dissolution-assisted extensional crack. This is different from the stretching-induced fractures in SGC (see Zhu et al. 2016) where non-uniform precipitation is indispensable. The dissolution-assisted fracturing in LGC and the stretching-induced fracturing in SGC both generated secondary pore space during the experiments, but the fractures in LGC differs distinctively from those on SGC in many ways:

- Firstly, the dissolution-assisted fracturing is a single, planar feature in 3-D with no obvious secondary fractures branching out, while the fractures observed in the SGC sample formed a network of intersecting cracks. Figure 10a shows the morphology of the dissolution plane and the fracture network in 3D. It's shown in Figure 10b that the fractures intersected with each other and formed a complex wedge shape network with the vertex pointing towards the sample's interior. The dissolution-assisted fracturing mainly developed along a plane and show less intersection with other features.
- Secondly, the LGC sample dominated by dissolution features shows clear evidence for shrinkage of larger grains and disappearance of smaller grains at the interior of the aggregate (Figure 5a). The SGC sample exhibits patches that develop during the reaction which are evidences for the reaction product precipitation (Zhu et al., 2016).
- Thirdly, the development of micron-scale dissolution is simultaneous, with the shrinkage of grains occurring both at the surface and the interior of the cup wall (Figure 5 and 6a). In contrast, development of the reaction-induced fracturing is successive with most fractures occurred first at the surface and migrated towards the interior of the cup wall. This caused the observed wedge shape of the fracture network (Figure 10b). Development of the fractures also exhibits hierarchical sequence with main fractures appearing first. The secondary fractures branch out from the main fracture and divide the sample into smaller domains (Figure 2 from Zhu et al., 2016).
- What's more, no precipitates were observed along planar dissolution features in the LGC sample, the cup wall remains straight throughout the experiment. But for the SGC, the cup wall shows clear spalling which is a sign of non-uniform expansion that links to precipitation in this experiment.

### 3.5 Dissolution and fracturing of individual olivine grain

The reaction affected not only the aggregate but also the individual olivine grains. Both the dissolution and fracturing are observed at grain scale in the SGC sample. Figure 11 shows a series of image slices through a nanotomography dataset, moving through an olivine grain in the cup wall. The grains clearly exhibit channels (etch pits) in the reaction zone. In video S1 (supplementary materials) it can be seen that these channels penetrate into, and even through olivine grains. As we do not observe any precipitation filling or clogging the tubes, it is therefore reasonable to think that the channels start as etch-pits and grow deeper with the advancing of dissolution and eventually become the through going channels observed here. The tubular shape and the depth of penetration indicate that they are 'worm hole' features, likely resulting from dissolution. The shape and

the width of these channels vary, with wider inner channel diameters below the surface suggesting more extensive dissolution at depth. On average, most typical tubes have an inner diameter of around 720nm.

The fracturing is also observed on individual grains at nano-meter scale. Figure 12 shows nanotomographic evidence for hierarchical fracturing within olivine grains. The secondary fractures developed from the primary fracture and formed in a direction that is perpendicular to the earlier ones.

In the reconstructed microtomographic images of the loose grains from the SGC, we observed the precipitation of secondary minerals on the surface of the olivine grains inside the cup (Figure 13). On the basis of their rhombohedral shapes we identified these as magnesite crystals. However, the phase contrast between the precipitates and olivine grains is very small, and at the current spatial resolution of ~2 micron, we could not segment precipitates from olivine grain with acceptable uncertainties. Other minerals (e.g. serpentine, brucite, etc., see reaction 1~4) were likely also present in the sample, but could not be isolated at the given image resolution. Measurement of the magnesite circumference revealed continuous growth during the experiment (see Figure 5 in Zhu et al., 2016). The first magnesite crystals emerged after 48 hours, and grains kept nucleating and growing after that. Growth continued until the experiment was aborted and no deceleration could be observed at any point, which indicates that the sample continued reacting. We determined a growth rate for the grain perimeter of 0.772 $\mu m \cdot hour^{-1}$, which, by assuming cubic shape of the crystal yields an equivalent growth rate of $7.18 \times 10^{-3}$ $\mu m^3 \cdot hour^{-1}$. We used a density of 3.01 $g \cdot cm^{-3}$ and molar weight of 84.314 $g \cdot mol^{-1}$ for magnesite ($MgCO_3$) in our calculation. Assuming a specific reaction surface of $50 \times 50$ $\mu m^2$, this gave a magnesite growth rate of $2.85 \times 10^{-15}$ $mol \cdot cm^{-2} \cdot s^{-1}$. This is in general in agreement with the calculation of Saldi et al. (2009).

The volume change of a loose olivine grain inside the cup was calculated to quantify the competing effect of dissolution and precipitation during olivine carbonation. Individual grains were labelled from the segmented data, and their volumes determined. Figure 13 plots the volume change of a single grain selected from the loose grains inside the SGC over 13 successive microtomographic datasets (covering 146 hours). Magnesite overgrowth causes a significant roughening of the olivine grain surface. While the volume of the individual magnesite grain steadily increased throughout the reaction (Zhu et al., 2016), the total volume of the grain (olivine plus precipitates) fluctuates from time to time, which reflects variable rates both in the precipitation of magnesite as well as in the dissolution of olivine. A large drop in grain volume occurred at around 38 hours, which is consistent with a period of vigorous olivine dissolution. The largest continuous grain volume increase took place between 40 to 70 hours, caused by the precipitation of magnesites. At ~70 hours, the grain volume again decreased considerably, indicating that dissolution became dominant once more. This second dissolution episode coincides with the appearance of reaction-induced fractures in the aggregate wall at ~68 hours, suggesting a positive feedback process.

## 4 Discussion

We claim that our experimental observations indicate the activity of two different mechanisms that both create fluid pathways effectively. These are dissolution-dominated fluid pathway generation at micro-meter scale in the case of the LGC experiment and at nano-meter scale in the case of SGC, and reaction-induced fracturing in the case of the SGC. We detail our interpretation in the following sections.

### 4.1 Dissolution and etch-pitting

Dissolution and etch-pitting are important mechanisms that affect the grains' surface morphology and the permeability of the sample (e.g. King et al., 2010; Røyne and Jamtveit, 2015). The nanotomographic observation, that etch-pitting incurs extensive

dissolution beneath grain surfaces, was also documented by Lisabeth et al. (2017a, 2017b) during the carbonation of dunites. Peuble et al. (2018) also observed nano-meter scale veinlets forming oblique to sub-vertical channels in partially-carbonated olivine grains during percolation experiment. The hollowing out of olivines seems especially important in areas where the grain boundary porosity is decreasing due to the precipitation of secondary minerals. There, subsurface dissolution channels in olivine grains preserve important fluid pathways and maintain the reaction. This supports the hypothesis of Andreani et al. (2009) that the permeability can be maintained by the preferential dissolution even in cases where the overall porosity is decreasing. Apart from providing access for fluids, subsurface dissolution features also make the grain more susceptible to fracturing and thereby promote the generation of fracturing observed in the experiment.

The permeability of these dissolution channels was calculated using Hagen–Poiseuille's Law (Poiseuille, 1844) and Darcy's Law (Darcy, 1856). Hagen–Poiseuille's Law allows the calculation of the fluid flow inside a tube in dependency of the pressure gradient:

$$Q = \frac{-\pi r^4}{8\eta} \frac{\Delta P}{\Delta L},$$ (1)

where Q is the volume flow/rate of discharge, r is the radius of the tube, $\eta$ is the viscosity of the fluid, $\Delta P$ is the pressure difference over the flow length $\Delta L$. Darcy's Law stated that the rate of discharge is proportional to the viscosity of the fluid and the pressure drop over a given distance, i.e., for a tube with a radius in r:

$$Q = \frac{-k\pi r^2}{\eta} \frac{\Delta P}{\Delta L},$$ (2)

where $k$ is the permeability of the tube. Combining the two equations, $k$ can then be derived as:

$$k = \frac{r^2}{8},$$ (3)

In this experiment, $r$ is ~6 pixels (360 nm). This yields a permeability of ~$1.6 \times 10^{-14}$ m$^2$, which is high enough to transmit reacting fluids through these channels. Considering the density of 'worm hole' features over the grain, the permeability contributed by the channels could be reduced by two orders of magnitude but is still able to transmit fluid.

These intragranular channels contrast the transgranular fractures. But the development of these etch-pitting dissolution channels also provide fluid path for the reaction and allow a more extensive degree of alteration of the grain. They weaken the grains, make them more susceptible to disintegration and provide nucleation sites of the later fracturing. While sparse in our data, we think that over geological time scales the contribution by dissolution channel to bulk permeability and the advance of the reaction would be significant. However, on the time scale of our experiments, these features alone are insufficient to explain the observed self-sustainability of the reaction considering the scale and density of the dissolution channels and we argue that the main contribution must come from volume mismatch cracking in our laboratory study.

**4.2 Reaction-induced fracturing**

Olivine carbonation could produce up to 44% increase in solid molar volume assuming the reaction can proceed to completion. If such a volume increase takes place, the crystallization pressure generated could be high enough to fracture the host rock (Kelemen et al., 2013; Kelemen and Hirth, 2012). However, experimental studies on olivine carbonation show no evidence of high crystallization forces (van Noort et al., 2017) but rather suggest that precipitation causes the pore space to fill up and halt

the reaction before the crystallization induced pressure reaches the critical value needed to generate fracture (Hövelmann et al., 2012; van Noort et al., 2017). Our quantitative estimates indicate that in these experiments, the maximum volume expansion is ~5%. This is not enough to break the host rock, as shown in salt crystallization experiments (Scherer, 2004). Indeed, the nanotomography data show only dissolution features such as etch pits and worm holes, with no evidence of cracks in olivine grains surrounded by precipitates (Figure 11). The lack of evidence for crystallization pressure-induced cracking is consistent with other experimental studies (e.g. Hövelmann et al., 2012).

Based on a microtomography experiment, Zhu et al. (2016) proposed an alternative fracturing mechanism during olivine carbonation where crystallization pressure is not high enough to directly break the host rock. In their experiment, the observed fracture patterns in SGC is analogous to desiccation cracks (e.g., Edelman, 1973; Plummer and Gostin, 1981). In Zhu et al., (2016)'s model, the loose olivine grains inside the cup act as precipitate traps that keep the surface of the cup wall relatively free of precipitation. In the interior of the cup wall though, away from the precipitate traps, the crystallization pressure builds up and causes expansion. While the crystallization pressure is too low to cause shear fracturing of the cup, the expanding cup wall interior stretches the surface of the cup wall and causes it to fail in tension and tear. This is facilitated by the near-constant surface area (which decreases slightly as a result of dissolution). In analogy with desiccation cracks, the resulting fractures form characteristic and systematic polygonal patterns: The first set of fractures intersect at right angles, and all subsequent fractures divide the sample into smaller polygonal domains with increasing intersection angles. Since the fracture pattern develops successively rather than simultaneously, the higher-order fractures form in a different stress geometry and as a result migrate perpendicular to the surfaces generated by the previous fracturing event.

To evaluate the potential of surface stretching as a fracture generating mechanism, we estimated the stress that could be produced by the volume-mismatch in the cup wall of SGC. We did so by identifying and tracking grains whose spatial coordinates (x, y, z) changed continually as the sample expanded. Distances between these grains were measured at different times. Our measurements indicate an average expansion of ~9.1 μm over a distance of ~260 μm from 7 hours to 125.9 hours after the start of the experiment. The results revealed an axial elongation of 2.78~4.71% in ~120 hours in the LGC sample. However, little to no expansion was observed at the near surface of the sample's cup wall. This would translate into an axial strain of ~0.03 of the outer layer in order to compensate the volume mismatch. The elastic moduli and strengths of the synthesized porous olivine aggregates are similar to weak sandstones. Using a Young's modulus of ~10 GPa yields extensional stresses generated due to the expansion of ~300 MPa, easily exceeding the tensile strength of the sample (~10MPa). Interestingly, our estimate of extensional stress generated by the volume mismatch is of the same magnitude to the stress from crystallization pressurization (e.g. Kelemen et al., 2013). For natural peridotite, Young's moduli range from 108 to 194 GPa (Christensen, 1966), tensile strength is 50 to 290 MPa and spall strength is ~58 MPa (He et al., 1996). An equivalent volume expansion of ~10% in nature could lead to a stress of 3.24 GPa. In both cases, the stress is more than sufficient to fracture the material. However, these are simple estimations of stress and strain made with basic assumptions and local conditions. Considering the extent of the local carbonation reaction and how the expansion in the center is affecting straining of the outer layers, the estimated stress can be considerably lower but should still be in a range that is sufficient to break the material.

To generate the expansion cracks via surface stretching, the volume mismatch must be substantial, which requires to keep the near surface region free of precipitates. Zhu et al. (2016) suggested that the loose olivine grains inside the sample cup worked as precipitate traps/attractors in this experiment. Because the rate of crystal growth decreases drastically as the curvature of the substrate increases (García et al., 2013; Ziese et al., 2013), large grains in general are preferred sites for precipitation of new crystals. With a size contrast of ~2 orders magnitude, the loose olivine grains (100-500 μm) in the immediate vicinity of the inner cup surface fulfilled the function of precipitate traps and thereby kept precipitation level at the surface of the olivine cup wall low.

We tested the idea of volume mismatch cracking by conducting the LGC experiment. Now the size contrast between the grains forming the aggregate in the cup wall and the loose grains inside the cup was significantly reduced, and we expected less efficient precipitate trapping, and consequently little to no reaction-induced cracks. The experimental results support this idea. The only planar features observed in the new microtomography experiment are planar dissolution assisted cracking (Figure 6 and 10a).

A detailed examination of the dissolution channel shown in Fig. 6 revealed no evidence of precipitates there. This places doubt on the crystallization pressure being responsible for fracturing during olivine carbonation. If not, what could be an alternative explanation for the observed fracturing? To further address this question, we examined the porosity evolution and distribution in the 3-D tomographic datasets.

Despite the histogram analysis revealed a bulk increase in the porosity of the cup wall during the experiment, the distribution of these newly generated pores was inhomogeneous in the sample (Figure 9 and 14). This perturbed the initially homogeneous porosity distribution.  This effect became particularly apparent in subvolume 2, which started to exhibit higher porosity where it was closest to the outer surface of the sample after 68 hours (see Video S2, S3, S4 for details). The difference in porosity distribution within the sample became more pronounced as the reaction proceeded, with porosity in the outer surface of the cup wall increasing while the porosity inside the cup decreased. In our interpretation, this change in the pore volume reflects a contrast in the precipitation rate where precipitation proceeded more slowly in the outer part compared to the inner part of the sample wall, leading to different rates of expansion and the generation of tensile stresses.

The 'expansion cracks via stretching' mechanism can explain the observed microstructure evolution in two subvolumes of SGC (Figure 4). Since subvolume 2 is located at the periphery of the cup, it would be fractured before subvolume 1 which locates in the center of the cup wall. This predict from the 'expansion cracks via stretching' is consistent with the observed distribution of pore space that most porous area locates close to the periphery. This mechanism also explains why the fractures tend to develop perpendicular to the reaction surfaces. Similar models relating the reaction generated stress and fractures has also been used to explain other exfoliation cracks (e.g. Blackwelder, 1925).

In summary, two fundamental observations from our experiments are inconsistent with the "crystallization pressure induced fracturing" model and form strong arguments against high crystallization forces (i.e., sufficient to break the surrounding rock) (Figure 11, 14). Firstly, if the cracks were generated directly by crystallization pressure, we should expect them to initiate in region with intense precipitation and porosity reduction. However, in the outer layer of our sample where the fractures are observed, no precipitates formed prior to the fracturing. Secondly, on the nanoscale, the channels formed by dissolution show hollow and smooth inner surfaces and no precipitation of magnesite (or any other minerals) which shows evidences of low crystallization pressure.

Our detailed analyses provide quantitative support to the "surface cracking via volume mismatch" model first proposed by Zhu et al. (2016). Previous experimental studies on olivine carbonation show that the crystallization force is low (van Noort et al., 2017), suggesting that breaking host rocks by crystallization pressure as in salt crystallization is unlikely which is in contrast with fracture networks that are commonly observed in naturally occurred serpentinized and carbonated peridotites (Iyer et al., 2008; Macdonald and Fyfe, 1985). We present a resolution to this conundrum by documenting a process that allows fracturing without a high crystallization force.

**4.3 Coupled-mechanisms of dissolution and precipitation-driven fracturing**

The findings of this study can be summarized in a mechanism that couples dissolution and precipitation during olivine carbonation. If dissolution and precipitation are heterogeneously distributed in a rock, non-uniform volume expansion can cause breaking of the host rock via surface stretching. In nature, heterogeneity in the porosity and permeability of a rock formation is common, which may cause non-uniform concentration of reaction and distribution of precipitation (Wells et al., 2017). As shown in our study, the resulting volume mismatch could lead to expansion fractures. The fractures provide new fluid pathways and expose fresh reactive surfaces to sustain the carbonation. In a long-term, fluid pathways may be provided by "worm-hole" etch pitting. Dissolution channels could deteriorate rock strength over longer time scales (Figure 15).

In a field study on serpentinization of peridotites at ocean ridges, Rouméjon and Cannat (2014) show that the reaction-induced fracturing occurs in the early stages of serpentinization (probably before 20% of serpentinization) while the rest of the volume increase is accommodated by the serpentine itself and dissolution processes dominate until completion of the reaction. Clearly, natural processes are more complex. Laboratory studies are not capable of simulating nature settings due to the vastly different length and time scale. Instead, we focus on understanding the underlying mechanism of porosity generation during olivine carbonation reaction. Using the coupled dissolution and fracturing model described above, we postulate that at the beginning of a carbonation reaction, dissolution plays an important role in maintaining porosity. As reaction progresses, no-uniform expansion of the rock due to precipitation could lead to fractures. Once the host rock is fractured, accelerated reaction takes place to achieve 100% carbonation.

In general, several different mechanisms seem to facilitate olivine carbonation and contribute to sustaining it. On relatively short time scales, rapid reaction-induced tensile fracturing could be the dominating mechanism that maintains the reaction, whereas on a longer timescale, dissolution and the formation of channel-like structures may dominate.

**5 Conclusions**

Using synchrotron-based micro- and nano-tomography, we documented and quantified the reaction progress during olivine-fluid interaction on the micron scale. This allowed us to identify mechanism that sustain the reaction despite its large positive volume change.

In summary, our experiment results suggest:

- The reaction-induced fracturing observed in our experiments results from non-uniform volume expansion. Tensile stresses arise from heterogeneous precipitation and the resulting contrast in the expansion between a faster expanding interior and a slower expanding near-surface.
- Even though the dissolution cannot be used alone to explain the sustainability of the experimental-time-scale olivine carbonation, it provides evidence that dissolution etch-pits can provide fluid path and fresh reaction surface for the reaction to proceed. This helps in explaining the naturally occurring complete alteration of peridotite, as the time scale for natural carbonation ranges from thousands to million years. Even if the dissolution channelizing would only allow slow fluid flow, it could still induce significant alteration given time.
- The coupled-mechanism of dissolution and reaction-induced fracturing accounts for maintaining the reaction processes during olivine carbonation. It explains on different time and space scale about the formation of observed natural outcrops of completely carbonated peridotite.
- The results from our experimental study also provide new insights into the application of $CO_2$ mineral sequestration.

480 **References**

Andreani, M., Luquot, L., Gouze, P., Godard, M., Hoise, E. and Gibert, B.: Experimental Study of Carbon Sequestration Reactions Controlled by the Percolation of CO -Rich Brine through Peridotites, Environ. Sci. Technol., 43(4), 1226–1231, doi:10.1021/es8018429, 2009.

Bedford, J., Fusseis, F., Leclère, H., Wheeler, J. and Faulkner, D.: A 4D view on the evolution of metamorphic dehydration
485 reactions, Sci. Rep., 7(1), doi:10.1038/s41598-017-07160-5, 2017.

Beinlich, A. and Austrheim, H.: In situ sequestration of atmospheric CO 2 at low temperature and surface cracking of serpentinized peridotite in mine shafts, Chem. Geol., 332–333, 32–44, doi:10.1016/j.chemgeo.2012.09.015, 2012.

Beinlich, A., Plümper, O., Hövelmann, J., Austrheim, H. and Jamtveit, B.: Massive serpentinite carbonation at Linnajavri, N-Norway, Terra Nov., 24(6), 446–455, doi:10.1111/j.1365-3121.2012.01083.x, 2012.

490 Blackwelder, E.: Exfoliation as a Phase of Rock Weathering, , 33(8), 793–806, 1925.

Christensen, N. I.: Elasticity of Ultrabasic Rocks, J. Geophys. Res., 71(24), 5921–5931, doi:10.1029/JZ071i024p05921, 1966.

Cloetens, P., Barrett, R., Baruchel, J., Guigay, J. P. and Schlenker, M.: Phase objects in synchrotron radiation hard x-ray imaging, J. Phys. D. Appl. Phys., 29(1), 133–146, doi:10.1088/0022-3727/29/1/023, 1996.

Darcy, H.: Les fontaines publiques de la ville de Dijon, Recherche, 647 [online] Available from:
495 http://scholar.google.com/scholar?hl=en&btnG=Search&q=intitle:Les+fontaines+publiques+de+la+ville+de+dijon#0, 1856.

Deschamps, F., Godard, M., Guillot, S. and Hattori, K.: Geochemistry of subduction zone serpentinites: A review, Lithos, 178, 96–127, doi:10.1016/j.lithos.2013.05.019, 2013.

Eberhardt, E., Stimpson, B. and Stead, D.: Effects of Grain Size on the Initiation and Propagation Thresholds of Stress-induced Brittle Fractures, Rock Mech. Rock Eng., 32(2), 81–99, doi:10.1007/s006030050026, 1999.

500 Edelman, N.: Tension cracks parallel with the axial plane, 1973.

Emmanuel, S. and Berkowitz, B.: Suppression and stimulation of seafloor hydrothermal convection by exothermic mineral hydration, Earth Planet. Sci. Lett., 243(3–4), 657–668, doi:10.1016/j.epsl.2006.01.028, 2006.

Escartín, J., Hirth, G. and Evans, B.: Effects of serpentinization on the lithospheric strength and the style of normal faulting at slow-spreading ridges, Earth Planet. Sci. Lett., 151(3–4), 181–189, doi:10.1016/S0012-821X(97)81847-X, 1997.

505 Evans, B. W.: Metamorphism of alpine peridotite and serpentinite, Annu. Rev. Earth Planet. Sci., 5, 397–447, doi:10.1146/annurev.ea.05.050177.002145, 1977.

Falk, E. S. and Kelemen, P. B.: Geochemistry and petrology of listvenite in the Samail ophiolite, Sultanate of Oman: Complete carbonation of peridotite during ophiolite emplacement, Geochim. Cosmochim. Acta, 160, 70–90, doi:10.1016/j.gca.2015.03.014, 2015.

510 Fryer, P., Mottl, M., Johnson, L., Haggerty, J., Phipps, S. and Maekawa, H.: Serpentine bodies in the forearcs of western pacific convergent margins: Origin and associated fluids, in Geophysical Monograph Series, vol. 88, pp. 259–279., 1995.

Fusseis, F., Schrank, C., Liu, J., Karrech, A., Llana-Fúnez, S., Xiao, X. and Regenauer-Lieb, K.: Pore formation during dehydration of a polycrystalline gypsum sample observed and quantified in a time-series synchrotron X-ray micro-tomography experiment, Solid Earth, 3(1), 71–86, doi:10.5194/se-3-71-2012, 2012.

515 Fusseis, F., Xiao, X., Schrank, C. and De Carlo, F.: A brief guide to synchrotron radiation-based microtomography in (structural) geology and rock mechanics, J. Struct. Geol., 65, 1–16, doi:10.1016/j.jsg.2014.02.005, 2014a.

Fusseis, F., Steeb, H., Xiao, X., Zhu, W. L., Butler, I. B., Elphick, S. and Mäder, U.: A low-cost X-ray-transparent experimental cell for synchrotron-based X-ray microtomography studies under geological reservoir conditions, J. Synchrotron Radiat., 21(1), 251–253, doi:10.1107/S1600577513026969, 2014b.

520    García, N. A., Register, R. A., Vega, D. A. and Gómez, L. R.: Crystallization dynamics on curved surfaces, Phys. Rev. E - Stat. Nonlinear, Soft Matter Phys., 88(1), doi:10.1103/PhysRevE.88.012306, 2013.

Gislason, S. R., Wolff-Boenisch, D., Stefansson, A., Oelkers, E. H., Gunnlaugsson, E., Sigurdardottir, H., Sigfusson, B., Broecker, W. S., Matter, J. M. and Stute, M.: Mineral sequestration of carbon dioxide in basalt: A pre-injection overview of the CarbFix project, Int. J. Greenh. Gas Control, 4(3), 537–545, doi:10.1016/j.ijggc.2009.11.013, 2010.

525    Goff, F. and Lackner, K. S.: Carbon dioxide sequestering using ultramafic rocks, Environ. Geosci., 5(3), 89 LP-101, doi:10.1046/j.1526-0984.1998.08014.x, 1998.

Grandstaff, D. E.: Changes in surface area and morphology and the mechanism of forsterite dissolution, Geochim. Cosmochim. Acta, 42(12), 1899–1901, doi:10.1016/0016-7037(78)90245-4, 1978.

Gürsoy, D., De Carlo, F., Xiao, X. and Jacobsen, C.: TomoPy: A framework for the analysis of synchrotron tomographic data,
530    J. Synchrotron Radiat., 21(5), 1188–1193, doi:10.1107/S1600577514013939, 2014.

Hansen, L. D., Dipple, G. M., Gordon, T. M. and Kellett, D. A.: Carbonated serpentinite (listwanite) at Atlin, British Columbia: A geological analogue to carbon dioxide sequestration, Can. Mineral., 43(1), 225–239, doi:10.2113/gscanmin.43.1.225, 2005.

He, H., Jin, X., Jing, F. and Ahrens, T. J.: Characteristic of dynamic tensile fracture in augite-peridotite, in AIP Conference Proceedings, vol. 370, pp. 593–596, AIP., 1996.

535    Heilbronner, R. and Barrett, S.: Image Analysis in Earth Sciences, Springer Berlin Heidelberg, Berlin, Heidelberg., 2014.

Hövelmann, J., Austrheim, H. and Jamtveit, B.: Microstructure and porosity evolution during experimental carbonation of a natural peridotite, Chem. Geol., 334, 254–265, doi:10.1016/j.chemgeo.2012.10.025, 2012.

Iyer, K., Jamtveit, B., Mathiesen, J., Malthe-Sørenssen, A. and Feder, J.: Reaction-assisted hierarchical fracturing during serpentinization, Earth Planet. Sci. Lett., 267(3–4), 503–516, doi:10.1016/j.epsl.2007.11.060, 2008.

540    Jamtveit, B., Putnis, C. V. and Malthe-Sørenssen, A.: Reaction induced fracturing during replacement processes, Contrib. to Mineral. Petrol., 157(1), 127–133, doi:10.1007/s00410-008-0324-y, 2009.

Jamtveit, B., Kobchenko, M., Austrheim, H., Malthe-Sørenssen, A., Røyne, A. and Svensen, H.: Porosity evolution and crystallization-driven fragmentation during weathering of andesite, J. Geophys. Res. Solid Earth, 116(12), 1–12, doi:10.1029/2011JB008649, 2011.

545    Johannes, W.: An experimental investigation of the system MgO-SiO2 -H2O-CO2, Am. J. Sci., 267(9), 1083–1104, doi:10.2475/ajs.267.9.1083, 1969.

Kaestner, A., Lehmann, E. and Stampanoni, M.: Imaging and image processing in porous media research, Adv. Water Resour., 31(9), 1174–1187, doi:10.1016/j.advwatres.2008.01.022, 2008.

Kelemen, P. B. and Hirth, G.: Reaction-driven cracking during retrograde metamorphism: Olivine hydration and carbonation,
550    Earth Planet. Sci. Lett., 345–348, 81–89, doi:10.1016/j.epsl.2012.06.018, 2012.

Kelemen, P. B. and Matter, J. M.: In situ carbonation of peridotite for CO2 storage, Proc. Natl. Acad. Sci. U. S. A., 105(45), 17295–17300, doi:10.1073/pnas.0805794105, 2008.

Kelemen, P. B., Matter, J., Streit, E. E., Rudge, J. F., Curry, W. B. and Blusztajn, J.: Rates and Mechanisms of Mineral Carbonation in Peridotite: Natural Processes and Recipes for Enhanced, in situ CO 2 Capture and Storage, Annu. Rev. Earth
555    Planet. Sci., 39(1), 545–576, doi:10.1146/annurev-earth-092010-152509, 2011.

Kelemen, P. B., Savage, H. and Hirth, G.: Reaction-Driven Cracking During Mineral Hydration, Carbonation and Oxidation, in Poromechanics V, vol. c, pp. 823–826, American Society of Civil Engineers, Reston, VA., 2013.

King, H. E., Plümper, O. and Putnis, A.: Effect of Secondary Phase Formation on the Carbonation of Olivine, Environ. Sci. Technol., 44(16), 6503–6509, doi:10.1021/es9038193, 2010.

560     Lisabeth, H., Zhu, W., Xing, T. and De Andrade, V.: Dissolution-Assisted Pattern Formation During Olivine Carbonation, Geophys. Res. Lett., 44(19), 9622–9631, doi:10.1002/2017GL074393, 2017a.

Lisabeth, H. P., Zhu, W., Kelemen, P. B. and Ilgen, A.: Experimental evidence for chemo-mechanical coupling during carbon mineralization in ultramafic rocks, Earth Planet. Sci. Lett., 474, 355–367, doi:10.1016/j.epsl.2017.06.045, 2017b.

Macdonald, A. H. and Fyfe, W. S.: Rate of serpentinization in seafloor environments, Tectonophysics, 116(1–2), 123–135, 565     doi:10.1016/0040-1951(85)90225-2, 1985.

Mani, D., Nirmal Charan, S. and Kumar, B.: Assessment of carbon dioxide sequestration potential of ultramafic rocks in the greenstone belts of southern India, Curr. Sci., 94(1), 53–60, 2008.

Moore, D. E., Lockner, D. A., Summers, R., Ma, S. and Byerlee, J. D.: Strength of crisolite-serpentinite gouge under hydrothermal conditions: Can it explain a weak San Andreas fault?, Geology, 24(11), 1041–1044, doi:10.1130/0091- 570     7613(1996)024<1041, 1996.

Nasir, S., Al Sayigh, A. R., Al Harthy, A., Al-Khirbash, S., Al-Jaaidi, O., Musllam, A., Al-Mishwat, A. and Al-Bu'saidi, S.: Mineralogical and geochemical characterization of listwaenite from the Semail Ophiolite, Oman, Chemie der Erde - Geochemistry, 67(3), 213–228, doi:10.1016/j.chemer.2005.01.003, 2007.

van Noort, R., Wolterbeek, T., Drury, M., Kandianis, M. and Spiers, C.: The Force of Crystallization and Fracture Propagation 575     during In-Situ Carbonation of Peridotite, Minerals, 7(10), 190, doi:10.3390/min7100190, 2017.

Peuble, S., Andreani, M., Gouze, P., Pollet-Villard, M., Reynard, B. and Van de Moortele, B.: Multi-scale characterization of the incipient carbonation of peridotite, Chem. Geol., 476, 150–160, doi:10.1016/j.chemgeo.2017.11.013, 2018.

Plummer, P. S. and Gostin, V. a: Shrinkage cracks: desiccation or synaeresis?, J. Sediment. Petrol., 51(4), 1147–1156, doi:10.1306/212F7E4B-2B24-11D7-8648000102C1865D, 1981.

580     Poiseuille, J. L. M.: Recherches experimentales sur le mouvement des liquides dans les tubes de tres petits diametres, Imprimerie Royale. [online] Available from: https://www.irphe.fr/~clanet/otherpaperfile/articles/Poiseuille/%0Ahttps://www.irphe.fr/~clanet/otherpaperfile/articles/Poise uille/poiseuille1840a.pdf, 1844.

Power, I. M., Harrison, A. L., Dipple, G. M., Wilson, S. A., Kelemen, P. B., Hitch, M. and Southam, G.: Carbon Mineralization: 585     From Natural Analogues to Engineered Systems, Rev. Mineral. Geochemistry, 77(1), 305–360, doi:10.2138/rmg.2013.77.9, 2013.

Rouméjon, S. and Cannat, M.: Serpentinization of mantle-derived peridotites at mid-ocean ridges: Mesh texture development in the context of tectonic exhumation, Geochemistry, Geophys. Geosystems, 15(6), 2354–2379, doi:10.1002/2013GC005148, 2014.

590     Røyne, A. and Jamtveit, B.: Pore-Scale Controls on Reaction-Driven Fracturing, Rev. Mineral. Geochemistry, 80(1), 25–44, doi:10.2138/rmg.2015.80.02, 2015.

Rudge, J. F., Kelemen, P. B. and Spiegelman, M.: A simple model of reaction-induced cracking applied to serpentinization and carbonation of peridotite, Earth Planet. Sci. Lett., 291(1–4), 215–227, doi:10.1016/j.epsl.2010.01.016, 2010.

Saldi, G. D., Jordan, G., Schott, J. and Oelkers, E. H.: Magnesite growth rates as a function of temperature and saturation state, 595     Geochim. Cosmochim. Acta, 73(19), 5646–5657, doi:10.1016/j.gca.2009.06.035, 2009.

Scherer, G. W.: Stress from crystallization of salt, Cem. Concr. Res., 34(9), 1613–1624, doi:10.1016/j.cemconres.2003.12.034, 2004.

Singh, S. K.: Relationship among fatigue strength, mean grain size and compressive strength of a rock, Rock Mech. Rock Eng., 21(4), 271–276, doi:10.1007/BF01020280, 1988.

600     Ulven, O. I., Storheim, H., Austrheim, H. and Malthe-Sørenssen, A.: Fracture initiation during volume increasing reactions in rocks and applications for CO2 sequestration, Earth Planet. Sci. Lett., 389, 132–142, doi:10.1016/j.epsl.2013.12.039, 2014.

Velbel, M. A.: Dissolution of olivine during natural weathering, Geochim. Cosmochim. Acta, 73(20), 6098–6113, doi:10.1016/j.gca.2009.07.024, 2009.

605 Velbel, M. A. and Ranck, J. M.: Etch pits on naturally altered olivine from dunites of the Appalachian Blue Ridge Mountains, North Carolina, USA, Mineral. Mag., 72(1), 145–148, doi:10.1180/minmag.2008.072.1.145, 2008.

Wells, R. K., Xiong, W., Sesti, E., Cui, J., Giammar, D., Skemer, P., Hayes, S. E. and Conradi, M. S.: Spatially-variable carbonation reactions in polycrystalline olivine, Geochim. Cosmochim. Acta, 204, 252–266, doi:10.1016/j.gca.2017.02.003, 2017.

Weyl, P. K.: Pressure solution and the force of crystallization: a phenomenological theory, J. Geophys. Res., 64(11), 2001–
610 2025, doi:10.1029/JZ064i011p02001, 1959.

Wilson, M. J.: Weathering of the primary rock-forming minerals: processes, products and rates, Clay Miner., 39(3), 233–266, doi:10.1180/0009855043930133, 2004.

Wilson, M. J. and Jones, D.: Lichen weathering of minerals: implications for pedogenesis, Geol. Soc. London, Spec. Publ., 11(1), 5–12, doi:10.1144/GSL.SP.1983.011.01.01, 1983.

615 Winkler, E. M. and Singer, P. C.: Crystallization pressure of salts in stone and concrete, Bull. Geol. Soc. Am., 83(11), 3509–3514, doi:10.1130/0016-7606(1972)83[3509:CPOSIS]2.0.CO;2, 1972.

Zhu, W., Montesi, L. G. J. and Wong, T. F.: Shear-enhanced compaction and permeability reduction: Triaxial extension tests on porous sandstone, Mech. Mater., 25(3), 199–214, doi:10.1016/S0167-6636(97)00011-2, 1997.

Zhu, W., Fusseis, F., Lisabeth, H. P., Xing, T., Xiao, X., De Andrade, V. and Karato, S. I.: Experimental evidence of reaction-
620 induced fracturing during olivine carbonation, Geophys. Res. Lett., 43(18), 9535–9543, doi:10.1002/2016GL070834, 2016.

Ziese, F., Maret, G. and Gasser, U.: Heterogeneous nucleation and crystal growth on curved surfaces observed by real-space imaging, J. Phys. Condens. Matter, 25(37), doi:10.1088/0953-8984/25/37/375105, 2013.
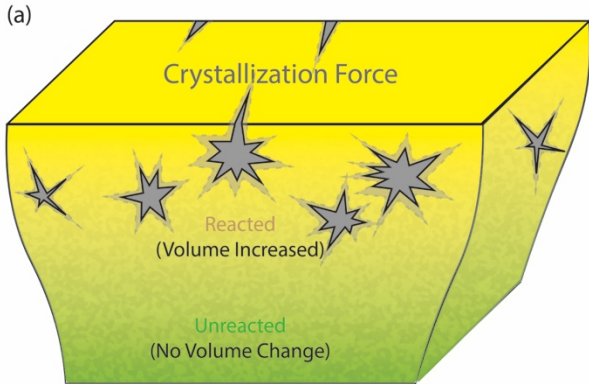
625
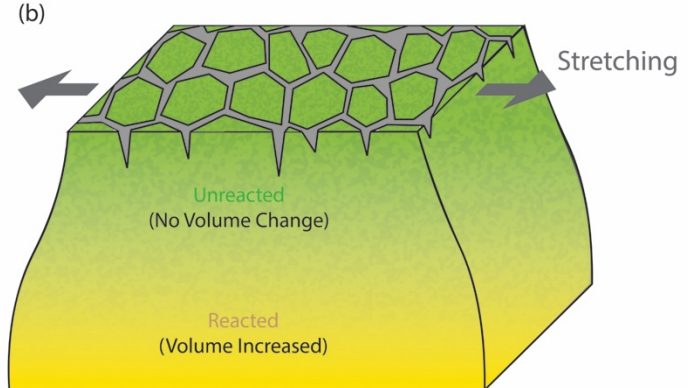
**Figure 1: Illustration of the mechanisms of reaction-induced fracturing during olivine-fluid interaction. a) The crystallization pressurization model describes the development of fractures caused by crystallization forces exerted on the surroundings due to growth of precipitates. Salt crystallization (Scherer, 2004) is a typical example of the crystallization pressure induced fracturing. The fractures first appear at areas where precipitation is most concentrated and propagate outwards. b) The surface cracking model**

630 **describes the development of fractures as a result of a contrast in expansion which causes stretching at the surface. A difference in the precipitation rate between the periphery and interior of the sample causes them to expand in different rates with the interior expanding faster than the surface. This builds up the tensile stress at the surface that fractures the sample and leads to a development of a polygonal fracture network. The fractures propagate from the surface inwards.**

635 **Figure 2: Illustration of sample configuration. a) The sample is composed a sintered olivine aggregate cup with loose olivine sand fillings (grain size 100-500 μm). Quantitative microtomographic analyses are conducted on the tangential (pink), radial (orange) and cross (blue) section of the sample. b) Example of the tomographic images that was used in the 2D examination of Zhu et al. (2016).**
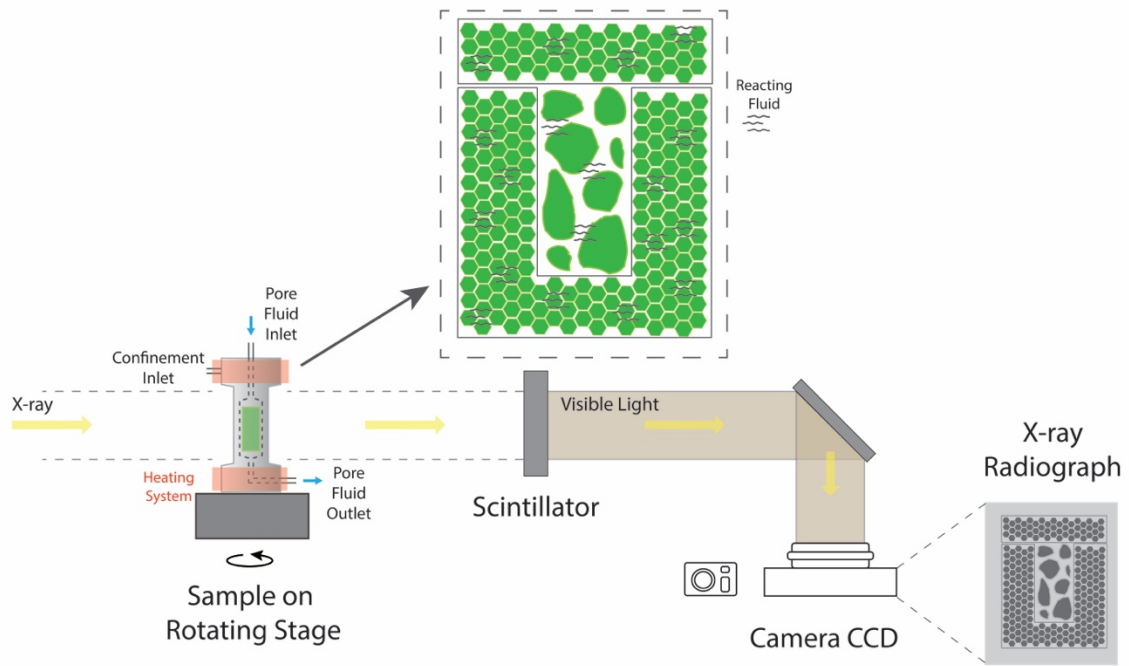
640 **Figure 3: Experimental setup for dynamic microtomography. Inside the x-ray transparent pressure cell, the confining pressure, pore pressure and temperature can be controlled independently. The synchrotron radiation imaging records radiographs of the sample at in-situ conditions with ongoing reaction at different angular positions with the sample being rotated.**
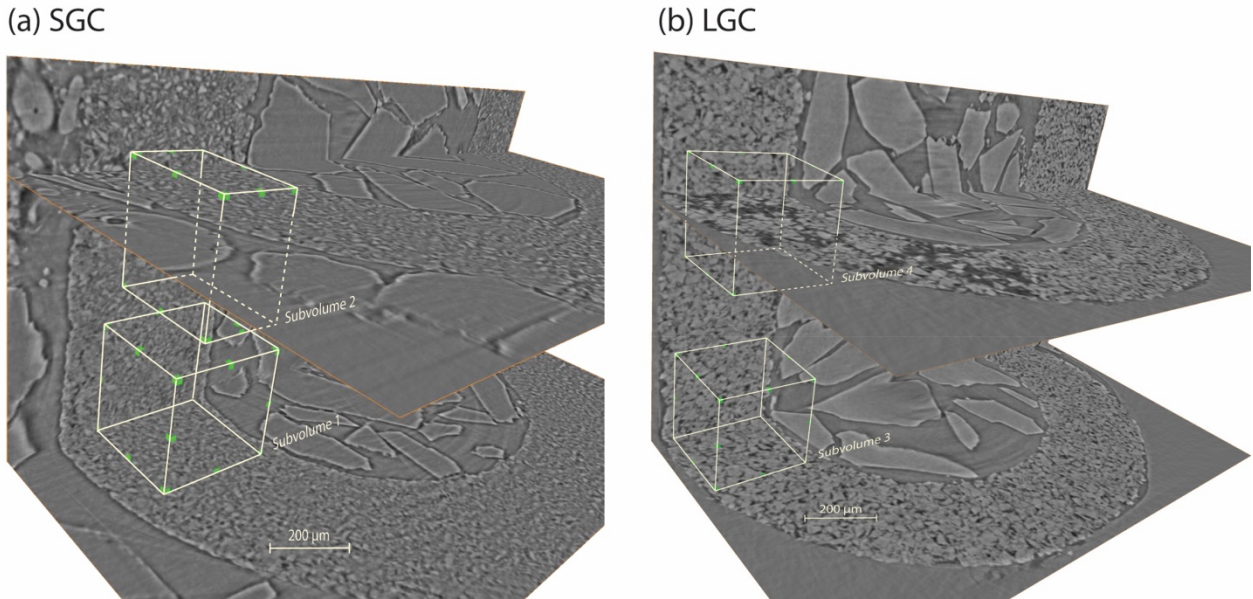
**Figure 4: Positions of the subvolumes in the cup wall of a) SGC and b) LGC, where quantitative 3D microstructure analyses were performed. In the SGC sample, subvolume 1 (bottom box) is located at the center of the cup wall. Subvolume 2 (top box) is located adjacent to the outer rim of the wall. In the LGC sample, both subvolume 3 (bottom box) and subvolume 4 (top box) are located at the center of the cup wall.**
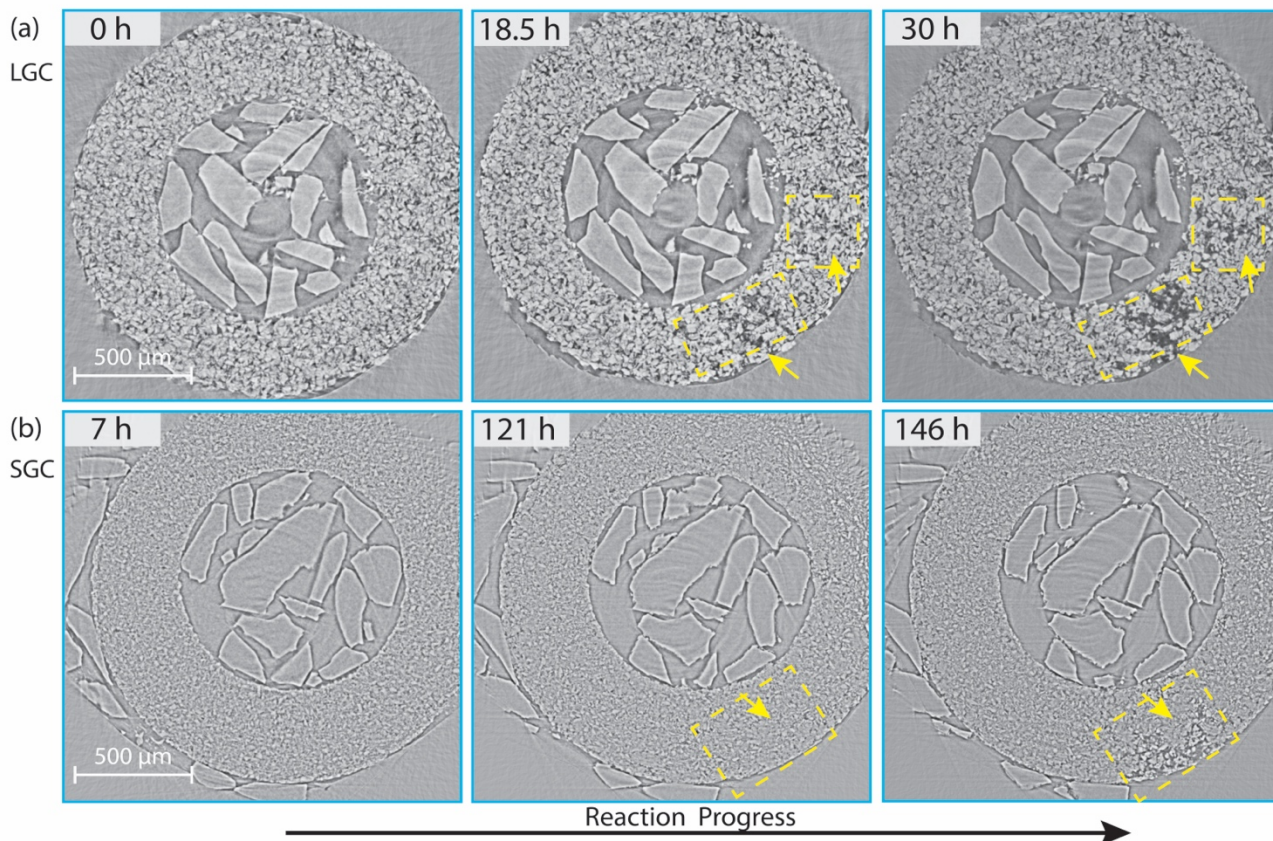
**Figure 5: Reconstructed images showing the cross section view of the sample undergoing olivine carbonation. a) In the LGC sample, original olivine grains shrink, and secondary pore space appears (yellow arrows), suggesting dissolution of olivine. Most of the large pore spaces concentrate at the interior of the cup wall (highlighted by yellow dash lines). b) In the SGC sample, the fractures first developed at the surface of the cup and propagated from the outer rim into the cup wall (highlighted by yellow dash lines). Larger pore space distributes mainly near the rim.**
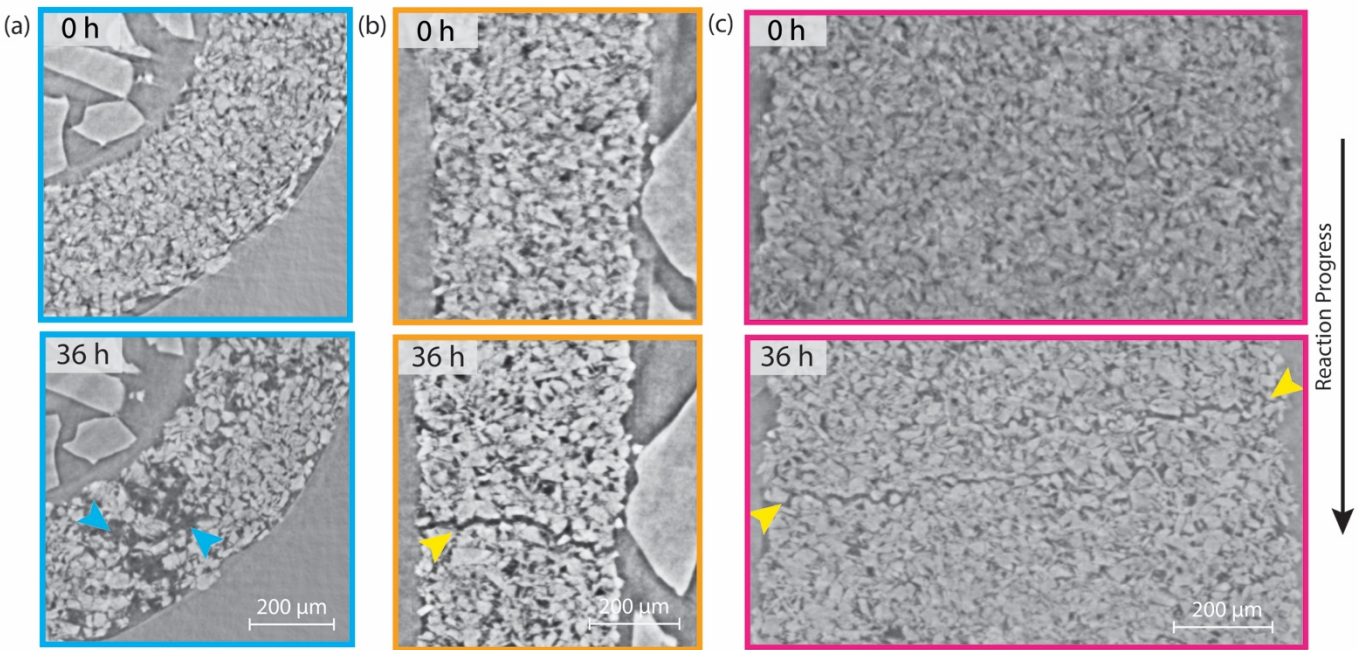
**Figure 6: a) Dissolution feature in the cross-sectional images of the LGC sample. 3D examination reveals that these dissolution features (blue arrowheads) are associated with planar fractures (yellow arrowheads) appeared in b) the radial and c) the tangential section images. The boarder color of each section corresponds to color code given in Figure 2.**
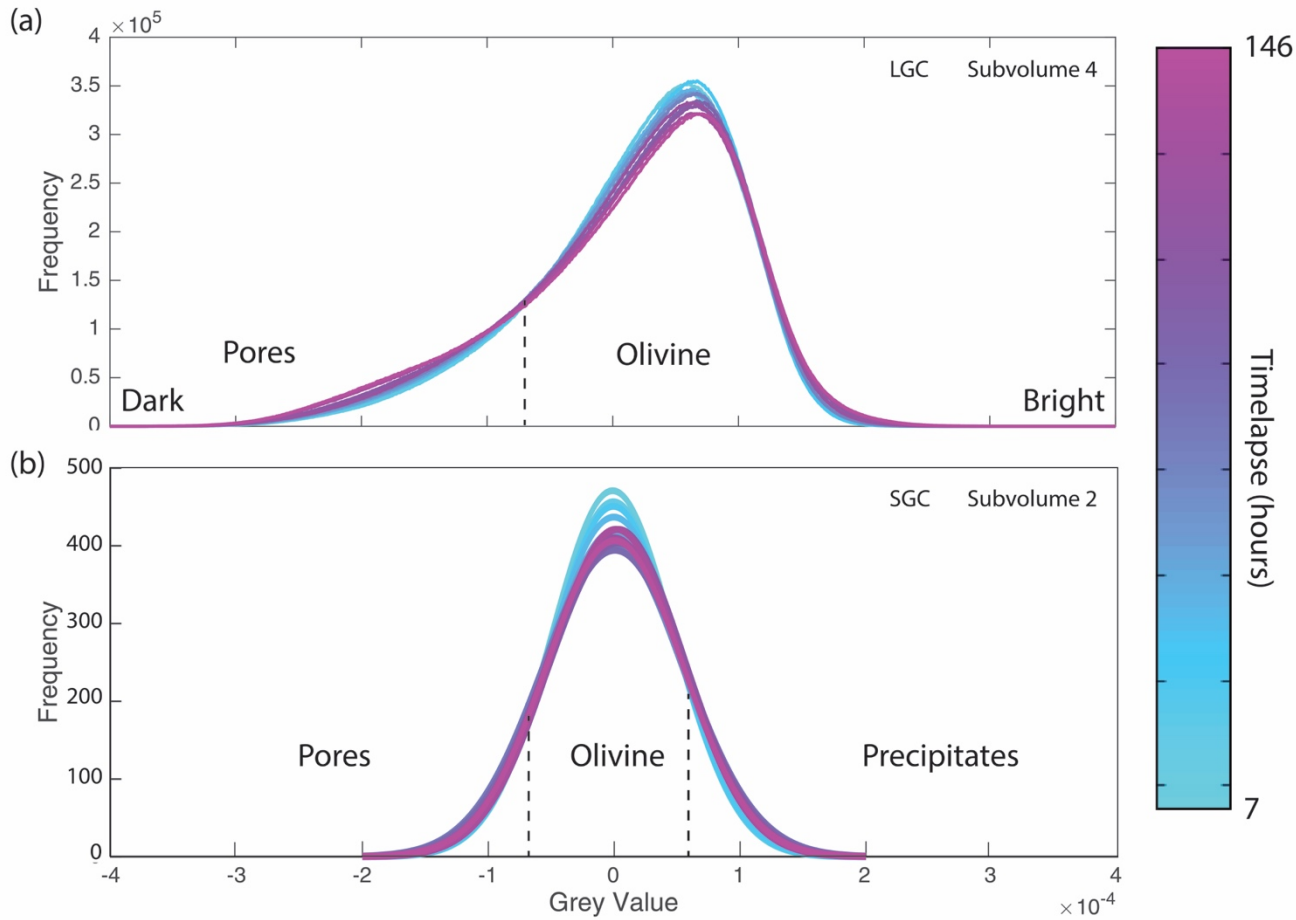
**Figure 7: Best-fits for the grey value distribution histograms of the sample at different stages of the reaction in a) subvolume 4 from LGC sample and b) subvolume 2 from SGC sample. Different colors represent time lapses as shown. Pores, olivine, and precipitates are identified based on their grey value ranges. Higher values correspond to lighter grey (solids). The more negative a value is, the darker the grey color becomes (e.g., pores are black). Histograms of SCG sample were calculated from a 2D image (Zhu et al., 2016), whereas the histograms of LGC sample were calculated from 3D datasets.**

660
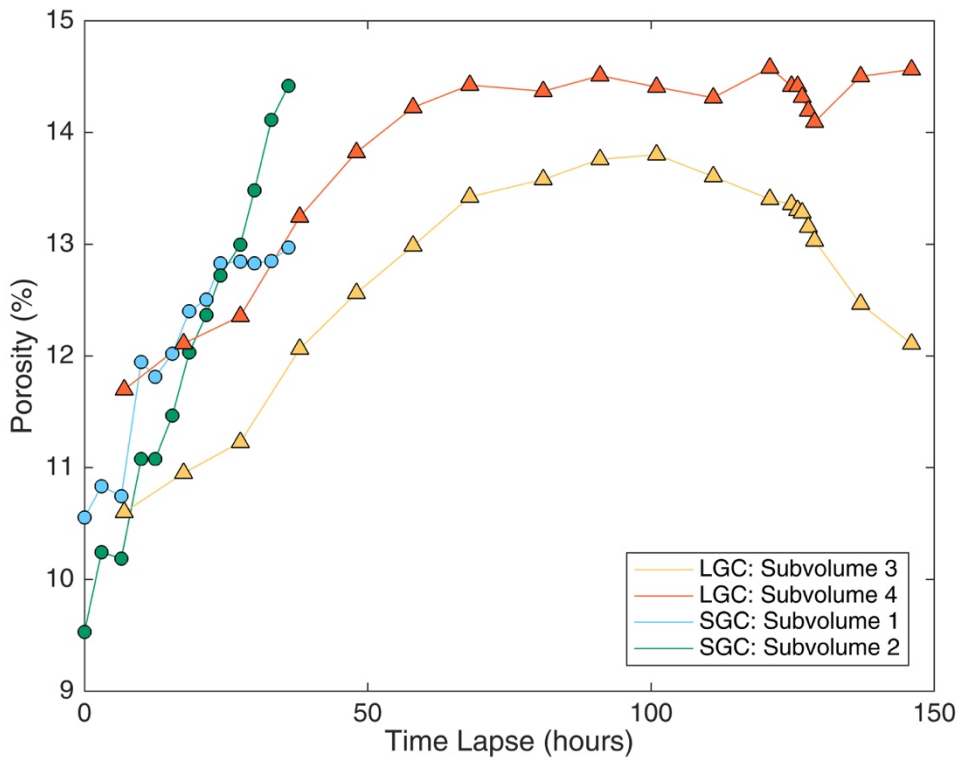
**Figure 8: Comparison of porosity evolution in LGC (this study) versus SGC reported by Zhu et al. (2016).**
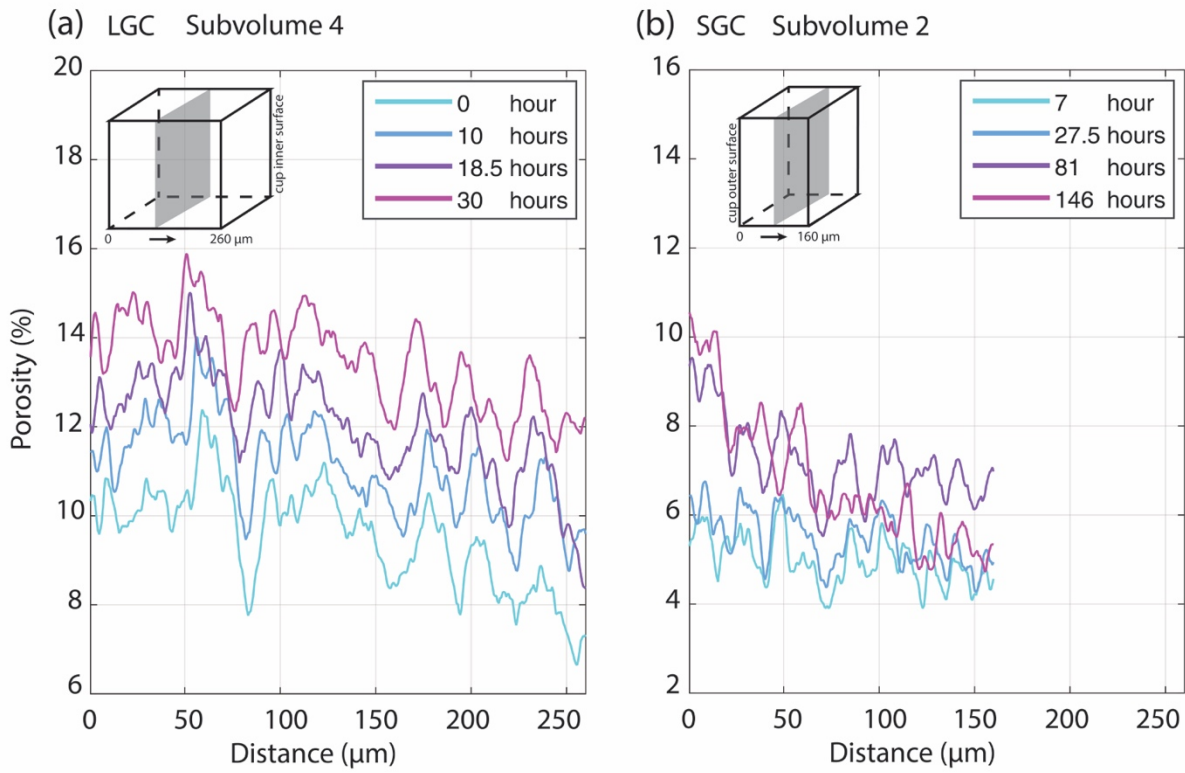
665

**Figure 9: Porosity profile of a) LGC and b) SGC along the radial direction of the sample cup. Different colors indicate reaction time lapse.**
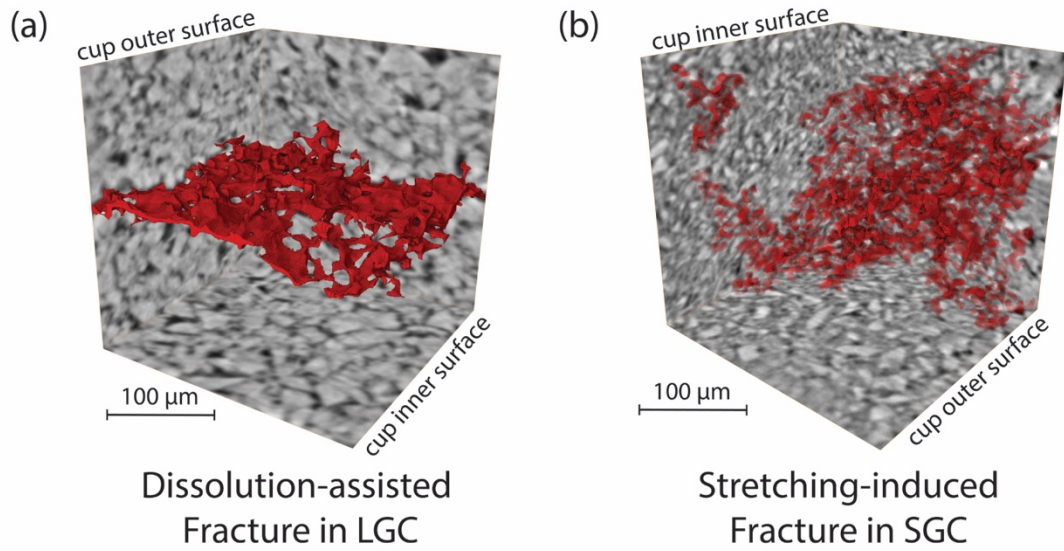
670 **Figure 10: The 3D geometry (in red) of a) dissolution-assisted fracture in LGC is distinctively different from b) the stretching-induced fractures in SGC. Both displayed volumes are 260×260×260 µm³ in size.**
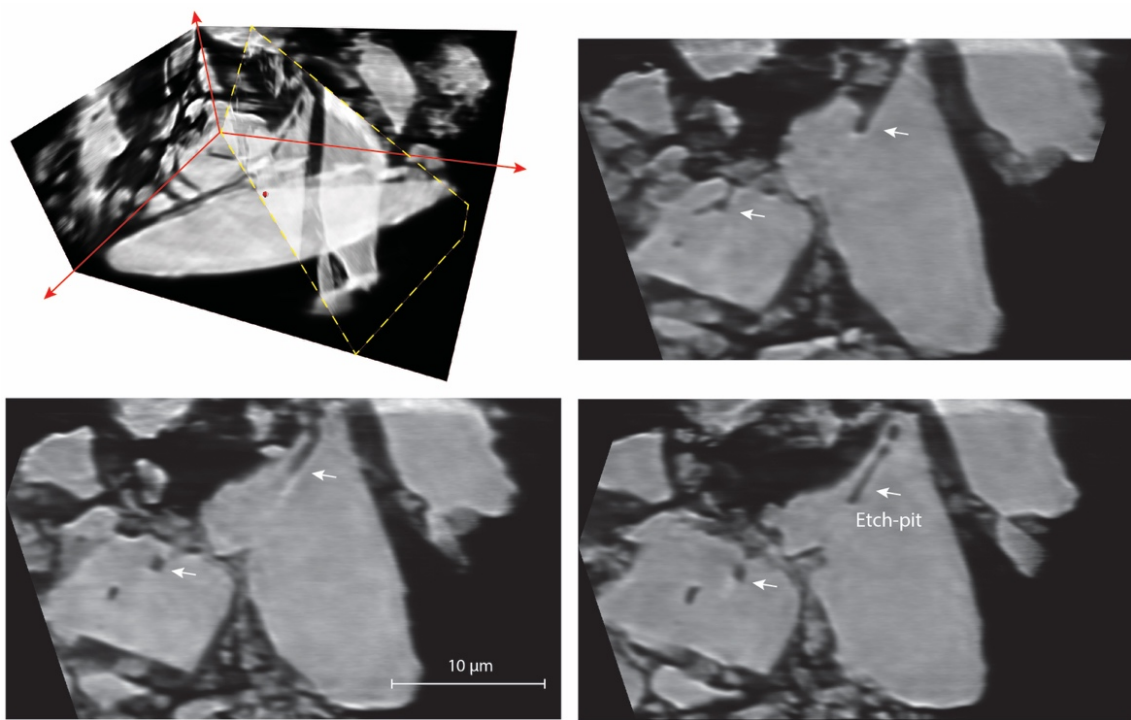
**Figure 11: Reconstructed images from the nanotomography data of the SGC sample's cup wall demonstrate the existence of etch-pits and dissolution channels (white arrows) formed in the olivine grain. The precipitates (darker grey) partially fill the pore space**
675 **(black) between olivine grains (lighter grey). The yellow dash line (in the upper left image) marks the orientation of the cross-sections (right and lower left images). The vertical distance between each 2D cross-section is ~600 nm. Reacting fluid causes a preferential dissolution of the grain which develops small channels that dig into the grain. These features provide a fluid path and eventually break grains, exposing new reactive surfaces.**
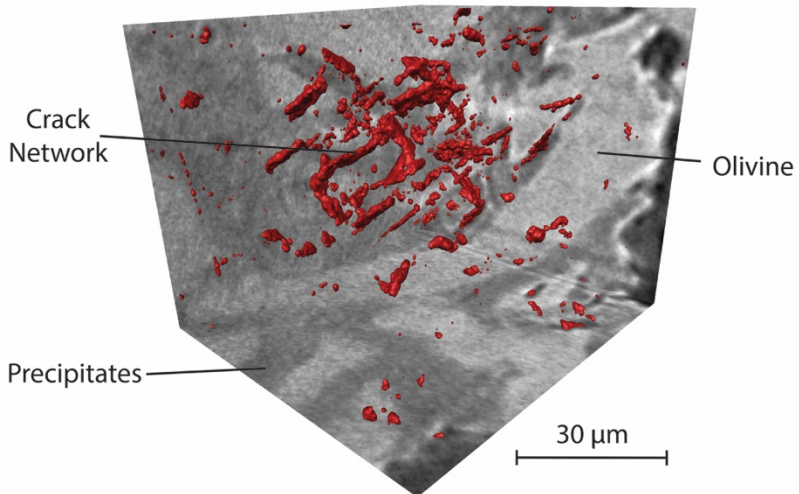
680 **Figure 12: Network of microcracks (red) in the reaction olivine cup wall from SGC shows a polygonal pattern. The dissolution channels make the grain (light grey) more susceptible and a stress concentration is also likely to occur around the etch pits.**
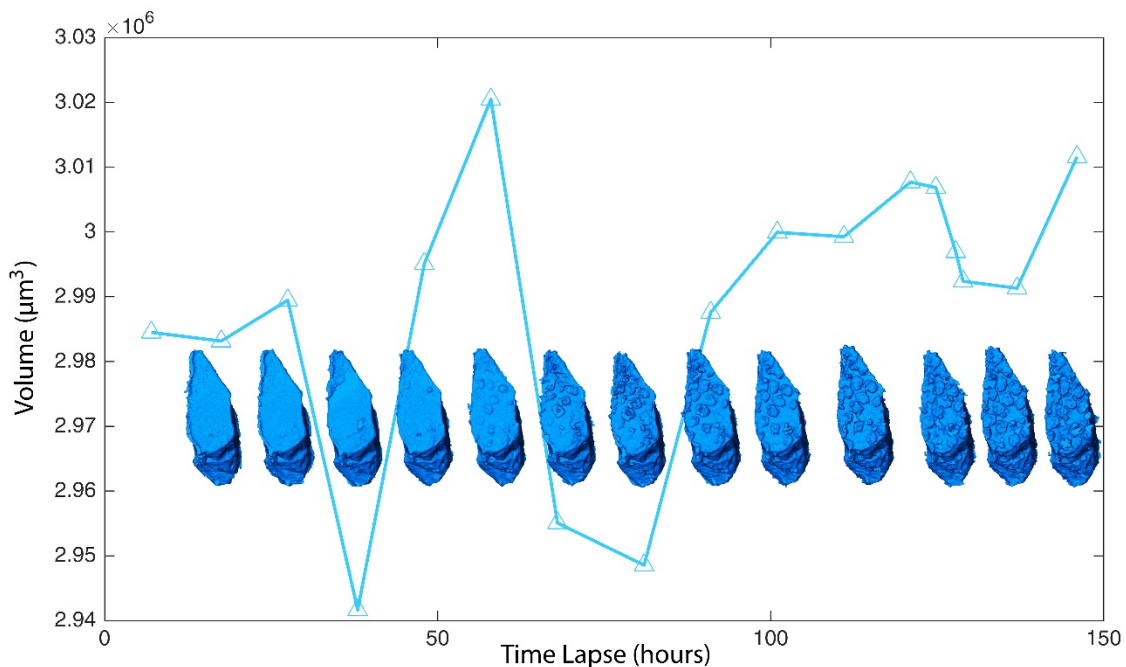
**Figure 13: Volume change of an individual olivine grain (total volume of olivine and precipitates) during carbonation reaction in the SGC experiment. The precipitates are idiomorphic and referred to as magnesites (see Zhu et al., 2016). This observed volume**
685 **change results from a combination of the dissolution of olivine and precipitation of magnesites. Fluctuations of the grain volume manifest the altering dominance of dissolution versus precipitation.**
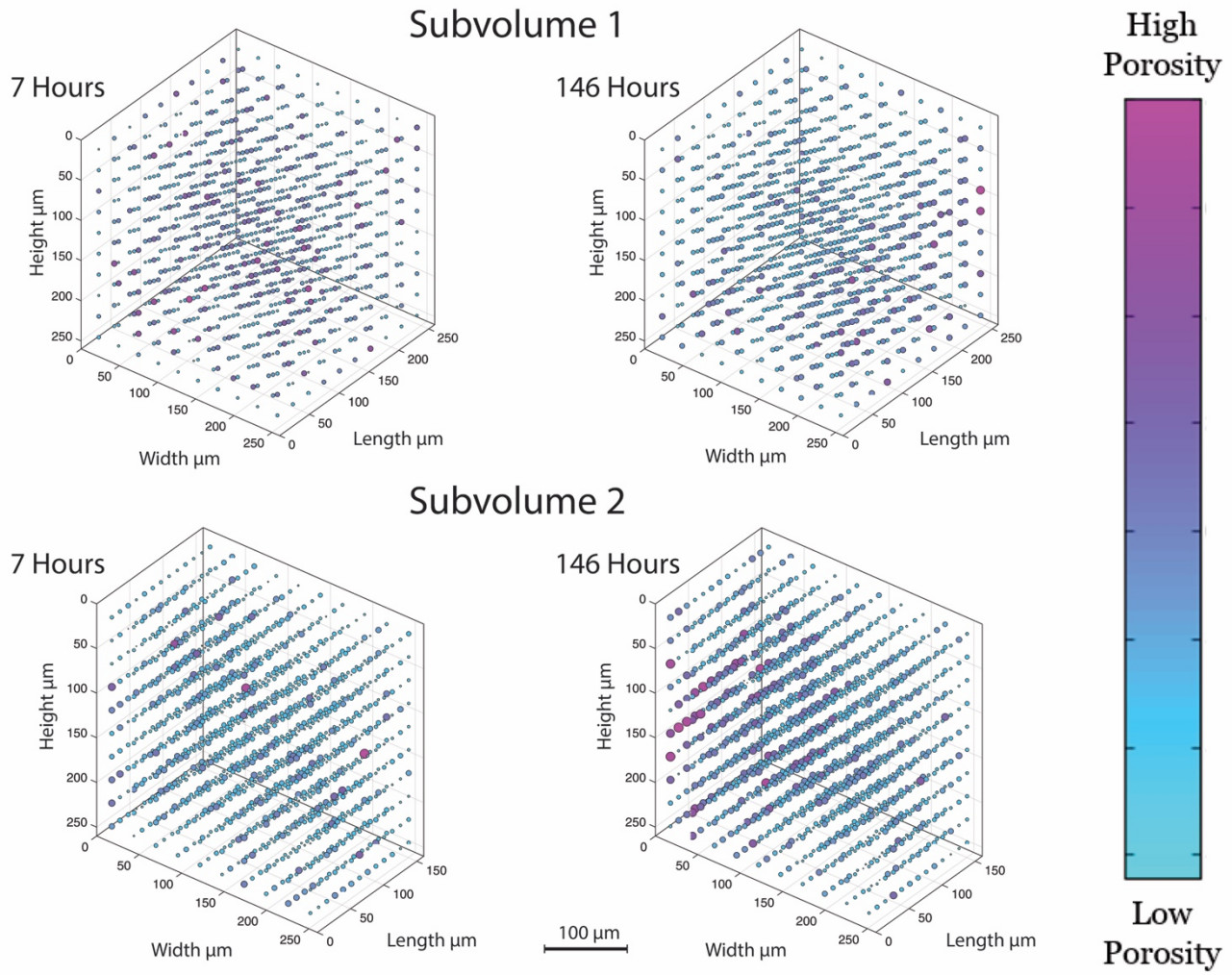
**Figure 14: Pores distribution within the subvolumes from SGC sample. For subvolume 1 which contains more inner part of the sample, porosity is relatively homogenous among the volume. For subvolume 2, as it contains more outer part of the sample, a concentration of high porosity can be found in the outer edge compare to the inner edge of the subvolume. This contrast in porosity also reflects a non-uniform precipitation which generates stress that fractures the rock.**

690
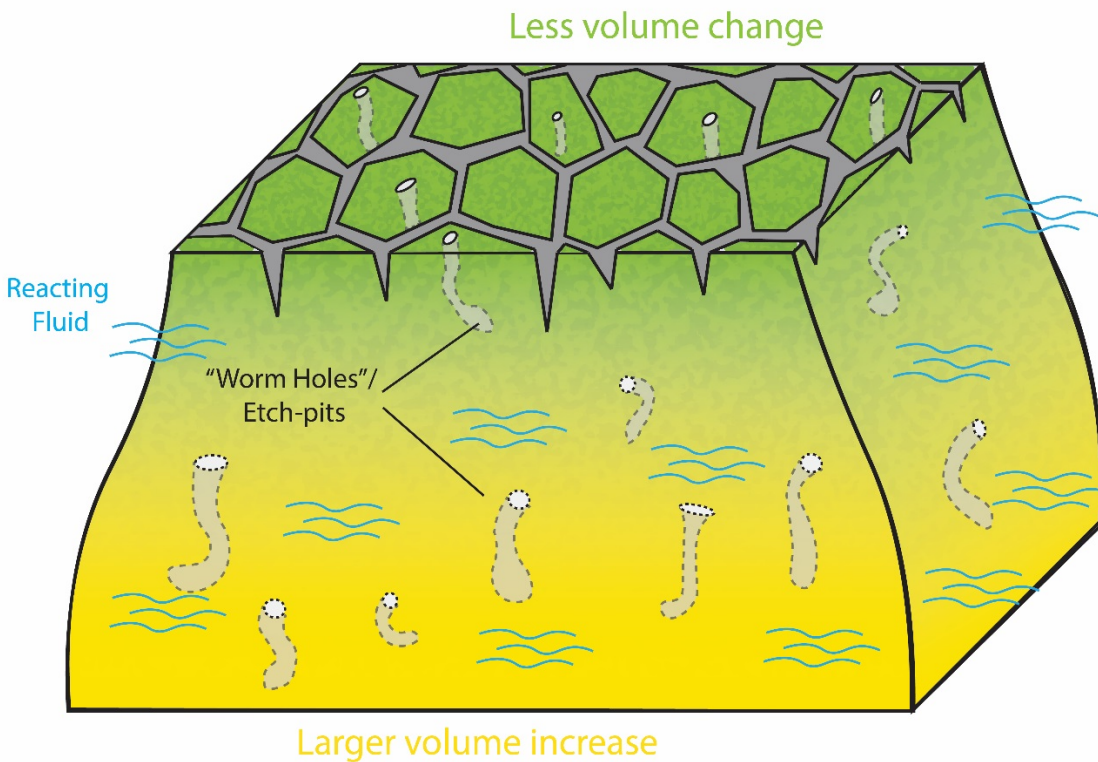
**Figure 15: Illustration of porosity generation mechanisms during the olivine carbonation reactions. A combined mechanism of surface cracking and the dissolution channelization plays an important role in the porosity generation. Heterogeneity in the microstructure of the material would cause non-uniform distribution of precipitation. This would lead to the generation of surface cracking via volume mismatch and generate secondary porosity. Dissolution also produces pore spaces and fluid pathways through etch-pitting channelization which makes the grains susceptible for the cracking on a longer time scale.**